ACS APPLIED MATERIALS & INTERFACES
Research Article
www.acsami.org

Hierarchical Mesoporous In_2O_3 with Enhanced CO Sensing and Photocatalytic Performance: Distinct Morphologies of $In(OH)_3$ via Self Assembly Coupled in Situ Solid−Solid Transformation

Arunkumar Shanmugasundaram,[†] Pratyay Basak,*[,†] Sunkara V. Manorama,*[,†] Binoy Krishna,[‡] and Srinath Sanyadanam[‡]

[†]Nanomaterials Laboratory, Inorganic and Physical Chemistry Division, CSIR-Indian Institute of Chemical Technology, Hyderabad-500007, Andhra Pradesh, India

[‡]School of Physics, University of Hyderabad, Hyderabad-500046, Andhra Pradesh, India

Supporting Information

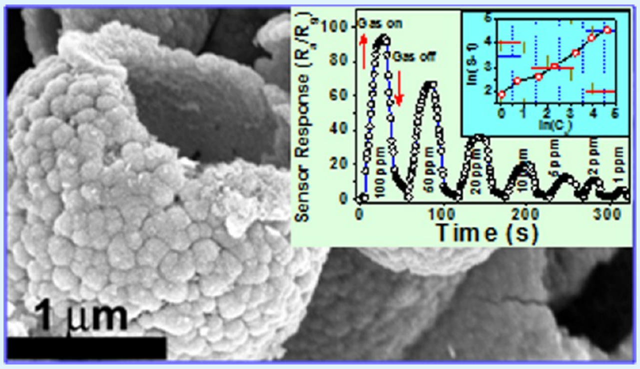

ABSTRACT: The present investigation details our interesting findings and insights into the evolution of exotic hierarchical superstructures of $In(OH)_3$ under solvothermal conditions. Controlled variation of reaction parameters such as, reactant concentration, solvent system, crystal structure modifiers, water content along with temperature and time, yielded remarkable architectures. Diverse morphologies achieved for the first time includes (i) raspberry-like hollow spheres, (ii) nanosheet-assembled spheres, (iii) nanoparticle-assembled spheres, (iv) nanocube-assembled hollow spheres, (v) yolk-like spheres, (vi) solid spheres, (vii) nanosheets/flakes, and (viii) ultrafine nanosheets. A plausible mechanism is proposed based on the evidence gathered from a comprehensive analysis aided by electron microscopy and X-ray diffraction studies. Key stages of morphological evolution could be discerned and rationally correlated with nucleation, growth, oriented attachment, and Ostwald ripening mediated by dissolution-redeposition mechanism coupled with solid evacuation. Remarkably phase-pure *bcc*-In_2O_3 with retention of precursor morphology could be realized postcalcination at 400 °C, which underlines the advantage of this strategy. Two typical hierarchical structures (raspberry-like hollow spheres and nanoparticles assembled spheres) were investigated for their gas sensing and photocatalytic performances to highlight the advantages offered by nanostructuring. An impressive sensor response, $S_{max} \approx 7340$ and 4055, respectively for the two structures along with appreciably fast response/recovery times over a wide concentration range and as low as 1 ppm exhibits the superior sensitivity toward carbon monoxide (CO). When compared to commercial In_2O_3, estimated rate constant indicates ∼3−4 times enhancement in photocatalytic activity of the substrates toward Rhodamine-B.

KEYWORDS: *hierarchical assembly, solid evacuation, hollow spheres, chemical sensing, photodegradation*

INTRODUCTION

As a unique class of materials inorganic hollow spheres have received significant attention, and its potential has been demonstrated in a wide range of applications.[1−3] The enormous interest in these materials arises from their distinctive structure, large surface area, low density, and superior electrochemical activities.[4] In the past decade, several stimulating methods have been developed for the preparation of exotic hollow structures,[5,6] that include well-known hard/soft templates,[7,8] emulsion[9] and selective etching.[10] Among these strategies, hard-templating is considered as the most reproducible technique, where the material is deposited on a solid core, which is later removed by either calcinations or chemical etching. However, the major bottleneck in this technique is the removal of the sacrificial templates which are generally complicated.[11,12] Developing a template free, facile, and simple method thus remains an exciting challenge for the researchers. Recent advances in synthesis strategies have demonstrated that hollow structures can be generated through direct solid evacuation mediated Ostwald ripening, Kirkendall effect, or both.[13−17] The findings have opened up newer possibilities to revisit and redesign the materials to yield superior properties.

Indium oxide (In_2O_3) is an important n-type semiconductor, with a reported optical band gap of ∼3.7 eV that includes the contributions from Burstein−Moss shift.[18] The excellent physicochemical and opto/electronic properties[19] have been successfully employed in several modern electronic devices.[20]

Received: January 20, 2015
Accepted: March 23, 2015
Published: March 23, 2015

DOI: 10.1021/acsami.5b00584
ACS Appl. Mater. Interfaces 2015, 7, 7679−7689

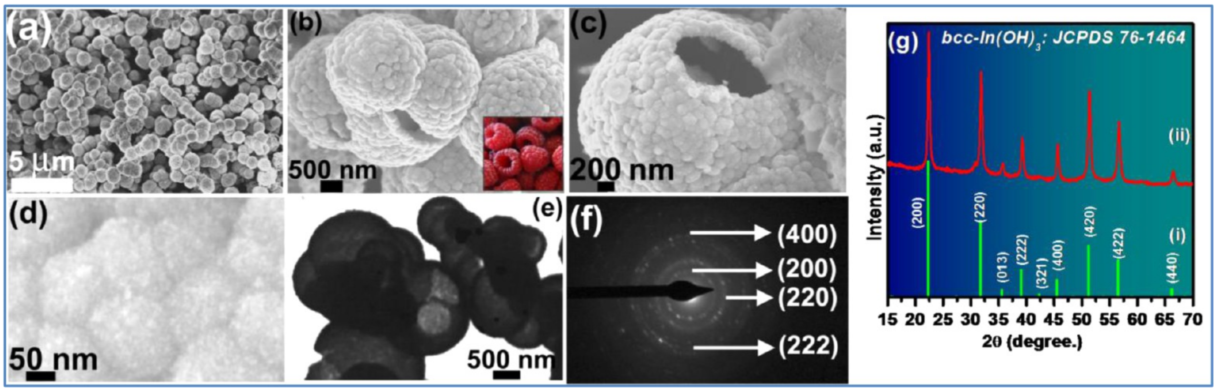

Figure 1. Electron microscopy images of raspberry-like $In(OH)_3$ architectures obtained at 220 °C for 24 h with 1:3 mol ratio of In^{3+}/OH^- in a DMF/ethanolamine/PEG volume ratio of 1:0.2:1; (a) panoramic image, (b−d) a series of high-magnification images highlighting the hierarchical raspberry-like assemblies. Inset in panel b: Typical photograph of raspberries. (e) TEM image of as prepared $In(OH)_3$ products, (f) the corresponding SAED pattern, and (g) powder X-ray diffraction pattern of (ii) as-prepared raspberry $In(OH)_3$ hollow spheres along with the standard X-ray diffraction pattern of (i) bcc-$In(OH)_3$ (JCPDS No. 76-1464).

Over the years several forms of In_2O_3 as nanowires,[18] nanotubes,[21] nanocubes,[22] nanosheets,[23] as well as other interesting hierarchical architectures,[24,25] have been realized and documented. Though, there have been several reports on In_2O_3 hollow spheres through template assisted methods,[26,27] to the best of our knowledge attempts toward template free synthesis has met with limited success.[28,29]

Herein, we demonstrate for the first time a successful strategy to generate a gamut of interesting hierarchical structures particularly raspberry-like hollow spheres of $In(OH)_3$ employing a facile solvothermal route notably without the use of any template. Comprehensive studies showcase the appreciable control that can be achieved on the material morphology by regulating simple but key reaction parameters, such as, reactant ratios, modifier to solvent concentration, temperature and time of the reaction. *N*−*N*-Dimethylformamide (DMF), a high boiling, strongly polar and high dielectric solvent is the medium of our choice. Ethanolamine is used as an organic Lewis base and a low molecular weight polyethylene glycol was used as a neutral structure modifier. Diverse morphologies of $In(OH)_3$ architectures obtained by the controlled variation of reaction medium ratio (DMF/EA/PEG) and In^{3+}/OH^- mole ratio includes (i) raspberry-like hollow spheres, (ii) nanosheet-assembled spheres, (iii) nanoparticle-assembled spheres, (iv) nanocube-assembled hollow spheres, (v) yolk spheres, (vi) solid spheres, (vii) flower-like nanosheets/flakes assembly, and (viii) ultrafine nanosheets. As a case study, a focused and systematic investigation was done to elucidate the formation mechanism of raspberry-like hollow spheres. The studies reveal that solid-evacuation mediated Ostwald ripening process extended in recent years, demonstrated for other metal oxides is indeed the solid−solid transformation pathway that generates these exotic architectures.[30,31] Finally, the *bcc*-In_2O_3 architectures retaining the morphologies of the corresponding $In(OH)_3$ precursors were obtained by calcining at 400 °C for 3 h under ambient atmosphere. The CO gas sensing properties of as prepared In_2O_3 architectures were evaluated as a function of sensing temperatures (T_s) $\leq$ 250 °C and gas concentrations (as low as 1 ppm) to demonstrate their enhanced performance. The sensitivity was found to be strongly dependent on the morphology and specific surface area of the In_2O_3 architectures. The excellent photocatalytic activity envisaged in these hierarchical In_2O_3 architectures is also exemplified in a parallel study on the degradation of a model organic dye, Rhodamine-B (RhB) under UV illumination.

EXPERIMENTAL SECTION

Chemicals. Indium chloride ($InCl_3$), indium(III) acetate ($In(C_2H_3O_2)_3$), indium(III) nitrate ($In(NO_3)_3$), *N*−*N*-dimethylformamide ($(CH_3)_2NCHO$), and polyethylene glycol (PEG, $M_n \approx 400$), were procured from Sigma-Aldrich, ethanolamine ($NH_2CH_2CH_2OH$), diethanolamine ($NH(CH_2CH_2OH)_2$), and 30% ammonia solution were obtained from sd fine-chem Ltd. All the chemicals were of analytical reagent (AR) grade and used without any further purification. Millipore deionized water (18.2 MΩ at RT) was used throughout the experiment.

Preparation of $In(OH)_3$ Hollow Spheres. In a typical synthesis procedure, 1 mmol (0.22 g) of $InCl_3$ and 3 mmol (54 μL) of water were dissolved in 25 mL of DMF under vigorous magnetic stirring, followed by slow dropwise addition of 5 mL ethanolamine. After the solution was stirred for 15 min, 25 mL of PEG-400 was added to the solution to get the final reaction mixture. The solution was transferred to a Teflon lined stainless steel autoclave and kept in a programmable oven. The temperature was ramped to 220 °C at a heating rate of 10 °C/min and the reaction allowed to proceed for 24 h. On completion of reaction time the autoclave was oven cooled. The product was recovered, centrifuged, washed several times with deionized water and ethanol to remove all residual impurities followed by drying at 60 °C. Several batches of experiments were sequentially carried out changing one parameter at a time employing similar protocols. The detailed reaction conditions and corresponding $In(OH)_3$ morphology are summarized in Supporting Information Table SI-1.

Preparation of In_2O_3 Nanostructures. The presynthesized white $In(OH)_3$ precursors were placed in a quartz crucible and calcined at 400 °C for 3 h in a conventional furnace under ambient atmosphere and pressure. The heating rate for the oven was maintained at 10 °C/min. After 3 h, the samples were oven cooled to obtain a pale yellow colored powder, which was confirmed by XRD to be In_2O_3.

RESULTS AND DISCUSSION

Morphology and Crystal Structure Evaluations: Initial Studies.

Figure 1 provides a series of electron micrographs of the product obtained in a typical solvothermal reaction, maintaining a (1:3) mole ratio of In^{3+}/OH^- in a mixed medium of DMF/ethanolamine/PEG (1:0.2:1, v/v ratio). The panoramic FE-SEM image (Figure 1a) evidently shows an even distribution of nearly monodispersed spheres of size ∼2 μm throughout the sample. The magnified images, Figure 1b and c clearly shows that each of these microspheres are actually

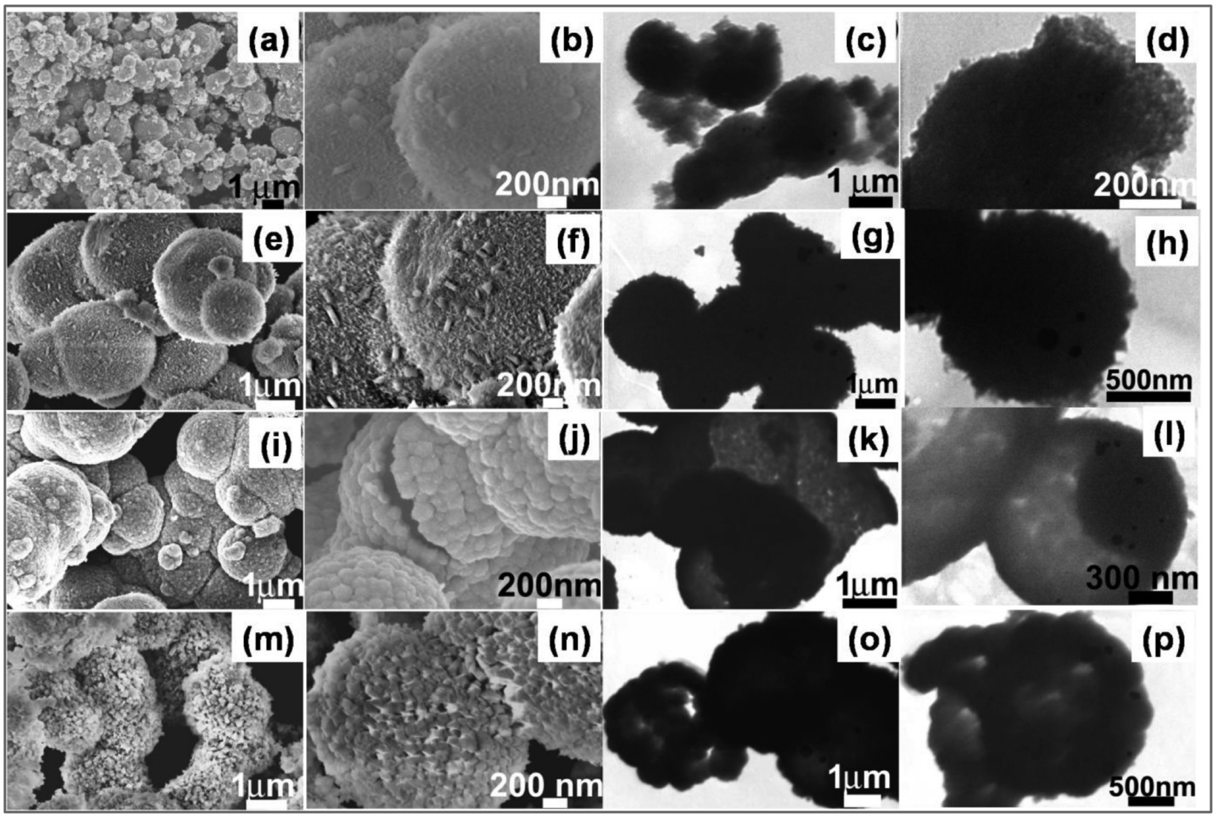

Figure 2. Morphological evaluations carried out using FESEM and TEM for the $In(OH)_3$ architectures obtained at 220 °C for 24 h with 1:3 mol ratio of In^{3+}/OH^- at different volume ratio of DMF/PEG at different magnifications: (a−d) 2:0, (e−h) 3:1, (i−l) 1:1, and (m−p) 1:3. As clearly evidenced, the corresponding $In(OH)_3$ hierarchical architectures formed are (a−d) spheres assembled spheres, (e−h) sheets assembled spheres, (i−l) raspberry-like hollow spheres, and (m−p) nanocubes assembled hollow spheres.

hollow and the skin is composed of several nanospheres with an average diameter of 200 nm, akin to raspberries (shown in inset). Interestingly, upon closer observation of these nanospheres under higher magnifications (Figure 1d), numerous ultrafine nanoparticles of size ∼10 nm are evidenced as the primary building blocks. The remarkable self-assembly of these ultrafine nanoparticles to form secondary structures (nanospheres) which reorganize hierarchically into an exotic tertiary architecture to finally yield raspberry-like hollow spheres under relatively benign conditions provided for a compelling motivation to carry out a comprehensive study. TEM studies (Figure 1e) further confirmed on the hollow interior with indications of yolk-like structures within. The SAED patterns with a series of diffraction rings and Laue spots (Figure 1f) indicated considerable crystallinity along with polycrystalline nature of the product. All the diffraction rings could be indexed to the *bcc*-crystal structure of $In(OH)_3$ with the space group of Ia_3 (204).[32,33] Crystal structure and phase purity of the samples were also investigated using powder X-ray diffraction as assigned in Figure 1g. The strongest signal derives from the {100} family of planes at $2\theta = 22.3°$ and corresponds to the reflection plane (200). The observation suggests ⟨100⟩ as a preferred direction for the $In(OH)_3$ crystal growth in these architectures. The calculated lattice parameters ($a = b = c = 0.797$ nm) conforms with the reported value (JCPDS card no.76-1464) of *bcc*-$In(OH)_3$ and absence of any contamination peaks indicated considerable phase purity.

Evolution of Morphologies: Dependence on Key Parameters. A series of controlled experiments were carried out to identify the role of key experimental variables that defines nucleation and crystal growth generating these exotic hierarchical structures. Systematic studies, involving composition of solvothermal medium, role of Lewis base, precursor to water ratio, effect of reaction time, temperature, and choice of precursor, collectively provided a rationale to comprehend the formation mechanism.

Effect of Solvothermal Reaction Medium. That the characteristics of the reaction medium plays a significant part is quite evident particularly in reference to our earlier study, where $In(OH)_3$ in cubic morphologies were obtained in hydrothermal conditions.[34] Dielectric strength and solvent polarity is expected to considerably affect the spatial orientation of planes and preferred direction of growth leading to distinct morphologies. The composition of solvothermal medium was hence varied in terms of DMF/PEG content while holding other reaction parameters constant. Figure 2 summarizes the findings through a series of scanning and transmission microscopy images that highlights the substantial change in morphology. In the absence of PEG, ultrafine primary particles of $In(OH)_3$ are seen to coalesce into micron sized spheres with fairly random size distribution. Supplementing 1/4th of the medium volume fraction with PEG, slight changes in the primary structures were visible which are predominantly InOOH. The primary structures appear to be nanosheet and nanoplate like morphologies aggregating into solid microspheres. Nevertheless, the significantly low degrees of crystallinity for these morphologies are apparent in the XRD (Supporting Information Figure S1). Interestingly, when DMF to PEG volume ratios were equal (1:1) a very noticeable change in the morphology was observed. An intricate self-

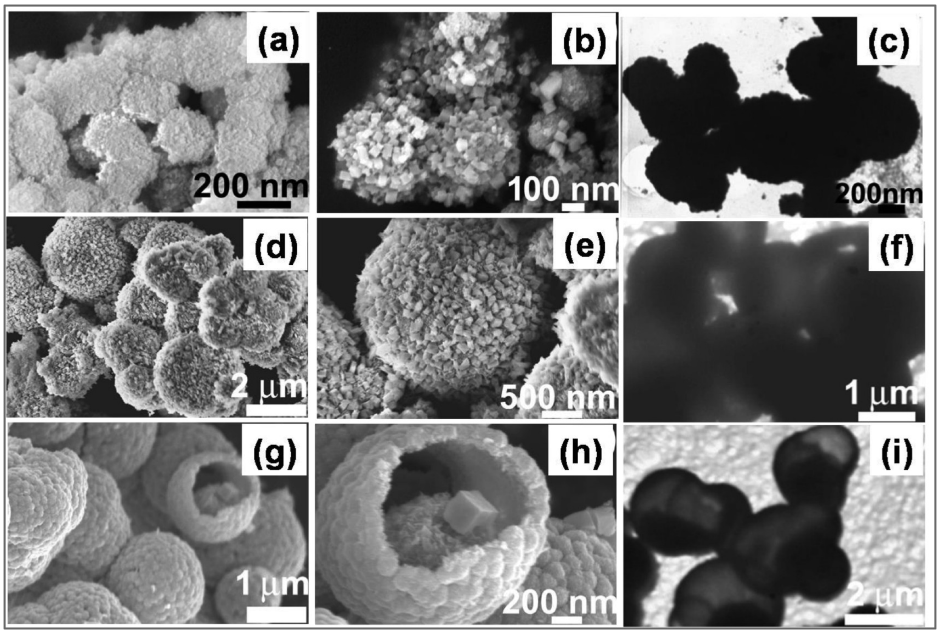

Figure 3. (a−i) Morphological evaluations of raspberry like $In(OH)_3$ hollow spheres as a function of time obtained at 220 °C with 1:3 mol ratio of In^{3+}/OH^- in 1:0.2:1 volume ratio of DMF/ethanolamine/PEG. The representative electron micrographs of the products collected at different stages of the reaction, (a−c) 1.5, (d−f) 12, and (g−i) 24 h.

assembly of ultrafine nanoparticles forming secondary nanospheres that reorganize hierarchically into hollow tertiary architectures (raspberry-like) is clearly witnessed. When PEG content is dominant, i.e. DMF/PEG (1:3), the secondary structures evidenced is deformed nanocubes (~200 nm). Both these hollow hierarchical assemblies are considerably monodisperse and comprise of phase pure crystalline $In(OH)_3$ as evident from the corresponding micrographs and diffraction patterns. Similar formation of nanoplate and cube-like architectures aided by polyethylene glycol was also demonstrated under hydrothermal conditions.[34] A medium devoid of DMF, shows random aggregation of the nanosheet/nanoplate like assemblies into ill-defined larger aggregates (Supporting Information Figure S2) which are again mixed phases of $In(OH)_3$ and InOOH (Supporting Information Figure S1).

Effect of Ethanolamine. The influence of ethanolamine as an organic Lewis base on the formation of the products was probed as a function of increasing concentration in the reaction medium, DMF/PEG (1:1) while maintaining other variables constant. In absence of ethanolamine, the obtained products (Supporting Information Figure S3) are of irregular sheet like morphologies comprising predominantly of InOOH as also evidenced from XRD (Supporting Information Figure S4). At a concentration when DMF/EA/PEG = 1:0.2:1, morphology of the products were invariably raspberry-like hierarchically assembled hollow spheres of phase pure $In(OH)_3$. By increasing the ethanolamine concentration, that is, DMF/EA/PEG = 1:0.4:1, although the raspberry morphology and $In(OH)_3$ phase was retained, the size of secondary structures are observed to be significantly reduced (Supporting Information Figure S3e−f). The change was also evident from the decrease in the degree of crystallinity in the corresponding XRD associated with significant peak broadening (Supporting Information Figure S4c). With further increase in ethanolamine in the reaction medium, the products obtained were wrapped nanosheet like morphologies as shown in the Supporting Information Figure S3g and h. A closer observation hints toward multiple node-like features for these sheet-like assemblies. The considerable presence of InOOH phase is clearly substantiated in the diffraction data collected for the sample (Supporting Information Figure S4d). When diethanolamine and ammonia were used as alternate Lewis base, ill-defined architectures of $In(OH)_3$ in irregular morphologies were obtained (Supporting Information Figure S5).

Effect of In^{3+}/OH^-. It is identified that presence of water is crucial to facilitate product formation in the solvothermal medium. A detailed study was undertaken to this effect with controlled variation of the water content, (In^{3+}/OH^-) in the reaction mixture and significant changes in the product morphologies (Supporting Information Figure S6) could be undoubtedly observed. Under water starved conditions (1:1.5 In^{3+}/H_2O mole ratio), the samples predominantly comprised of nanosheet assembled solid microspheres with decorations of smaller secondary aggregates atop them. The corresponding diffraction patterns (Supporting Information Figure S7a) indicated a mixed phase system. At ideal ratios, that is, 1:3, hollow spheres of raspberry-like morphologies were observed. With increasing water ratios, (1:6 and 1:12) the formation of secondary aggregates are seen to considerably diminish with a concomitant increase in the percentage of solid microspherical assemblies in the backdrop. The higher magnification clearly shows the yolk-like morphology. Significant increase in the InOOH phase under these conditions are also noticeable in the diffraction patterns provided in (Supporting Information Figure S7c and d). With considerably excess amount of water (>100 mol ratio) the products formed shows a urchin-like appearance comprising of ultrafine particles as the primary building blocks of the needles that assemble into solid microspherical geometries. The corresponding XRD (Supporting Information Figure S7e) confirms these samples to be comprised entirely of phase pure InOOH.

Effect of Reaction Time. The different stages of formation for raspberry-like hollow spheres were captured in a time dependent analysis that provided important clues toward determining the formation mechanism. The progress of reaction was arrested at various time intervals and the intermediate products so obtained were examined concurrently using electron microscopy (Figure 3, Scheme 1) and X-ray diffraction (Supporting Information Figure S9). Early stage of product formation, that is, at the end of 0.5 h, primary particles (~5−10 nm) formed (Supporting Information Figure S8a−c) coalesce into random spherical aggregates of ~200 nm. As observed from diffraction data (Supporting Information Figure S9a), these particles are predominantly in the InOOH phase. At one and half hour interval, a phase conversion along with typical shape transformation to $In(OH)_3$ is observed with cube-like structures (Figure 3a−c) decorated on the surface of secondary assemblies. With increase in the reaction time span both the secondary and tertiary assemblies grow in size, probably feeding on smaller particles, self-aggregating through Ostwald ripening and dissolution-redeposition mechanisms. The irregular cubic shapes of these secondary assemblies are very noticeable at the end of 6 (Supporting Information Figure S8d−f) and 12 h (Figure 3d−f). The high magnification image clearly shows that the spherical assemblies are very loosely constructed of the nanocubes defined with sharp edges. Another aspect that also starts to emerge at this stage is the appearance of an increasingly hollow interior as evident from the series of transmission electron micrographs. These observations are significant and have been proposed by several groups in recent years as the solid evacuation mechanism. As the aging process continues the nanocube edges appear smoother and the top layer apparently becomes more compact with increased particle-to-particle contact. The edges of secondary cubic aggregates are observed to slowly round off with increasing reaction time via this solid−solid transformation pathway. At the end of 24h, following prolonged reaction time the assemblies are seen to complete their growth with almost hollow interior to attain clusters of evenly monodispersed raspberry-like hollow spheres (Figure 3g−i). The intermediate and final diffraction analysis all show that the transformation to $In(OH)_3$ is retained with steady increase in the degree of crystalline ordering.

Scheme 1. Key Stages of Morphological Evolution for the Raspberry-like Hierarchical Superstructures Achieved[a]

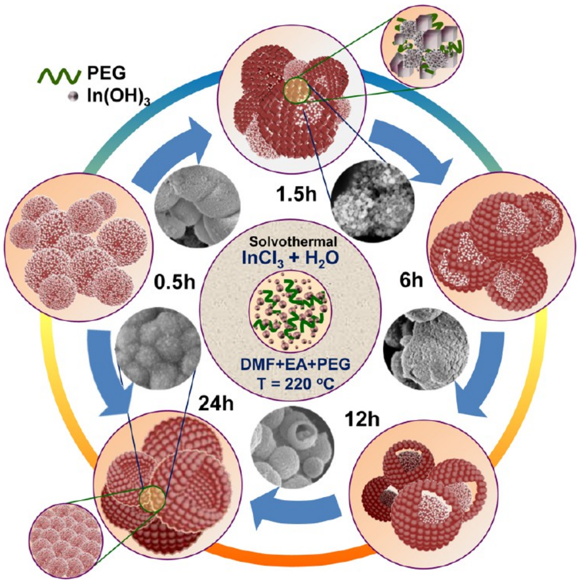

[a]The ultrafine nanoparticles (primary structures) self-assemble into secondary structures of spheres, transform into cube-like intermediate morphologies decorated on a spherical core, with time sharp edges of the cubes slowly rounds-off and evolves into spherical clusters. The final stages are associated with solid-evacuation of the interior along with Ostwald ripening of the secondary structures on the shell. Ultimately, the transformation lead to a compact tertiary superstructure that resembles the raspberry-like hierarchical architecture.

Effect of Temperature. Investigations were also carried out as a function of reaction temperature while keeping other reaction parameters same, that is, 1:3 mole ratio of In^{3+}/OH^- in DMF/EA/PEG (1:0.2:1) as the medium. The corresponding products (Supporting Information Figure S10) clearly showed a remarkable influence of the reaction temperature. When the solvothermal reaction temperature was 70 °C, only ultrafine nanoparticles of ~5−10 nm in mixed phase was obtained (Supporting Information Figure S10a and b). When the autoclave was held at 140 °C irregular shaped agglomerates (size ~1−2 μm) consisting of these primary structures were observed (Supporting Information Figure S10c and d). At 180 °C, formation of raspberry-like hollow spheres ~2 μm were noticed along with some irregular shaped smaller spheres indicating incomplete transformation of the morphology (Supporting Information Figure S10e and f). Finally, at reaction temperature of 220 °C, as discussed in the preceding section, nearly monodispersed raspberry-like hollow spheres were realized.

Effect of Indium Precursors. The effect of precursor was analyzed under similar reaction conditions of (1:3) mole ratio of In^{3+}/OH^- in DMF/EA/PEG (1:0.2:1) using indium nitrate and indium acetate as alternate starting materials. When indium acetate was used as the precursor, irregular nanocubes of size ~200 nm (Supporting Information Figure S11a and b) were obtained. The diffraction patterns clearly indicated formation of phase pure $In(OH)_3$ (Supporting Information Figure S12a). Polydispersed solid spheres of size ~1−2 μm (Supporting Information Figure S11c and d) were obtained when indium nitrate was selected as the indium source. The products were evidently a mixture of InOOH and $In(OH)_3$ (Supporting Information Figure S12b). Raspberry-like hollow spheres were exclusively obtained only when indium chloride was the precursor of choice.

Formation Mechanism. As discussed in preceding sections, the growth and temporal evolution of the product in solvothermal conditions were tracked under controlled variation of reaction parameters. On the grounds of these observations coupled with recent literature reports on similar attempts by several researchers,[35−38] a plausible mechanism on the formation and growth of these exotic $In(OH)_3$ hierarchical architectures can be rationally proposed. Ethanolamine as an organic base catalyzes the hydrolysis of metal-ion precursor, $InCl_3$, to initiate nucleation. At the same time, ethanolamine (Lewis base), PEG, and the Cl^- ions generated in situ can possibly control the nucleation and stabilize the $In(OH)_3$ seeds because of coordination effects.[39,40] The kinetics of these processes can undoubtedly differ considerably if the medium is altered.

Unlike hydrothermal reaction conditions,[34] however, the process of nucleation is observed to be much faster in the present case as evidenced in the time dependent evolution studies. Owing to faster nucleation rate, a supersaturated

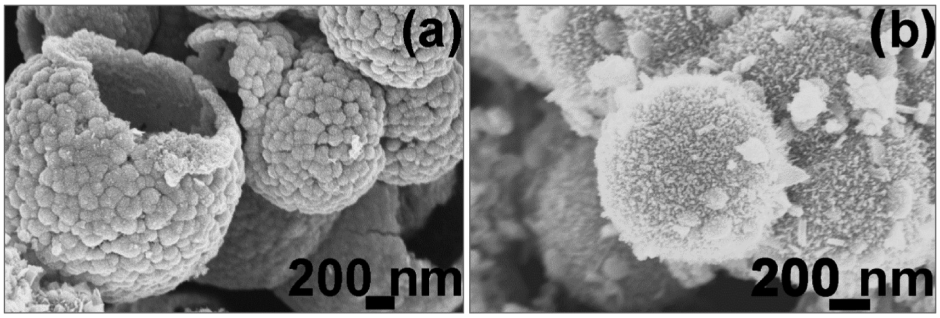

Figure 4. FE-SEM images of In_2O_3 (a) raspberry-like hollow spheres and (b) particles assembled spheres obtained after calcination of the corresponding $In(OH)_3$ precursors at 400 °C for 3 h under ambient pressure.

condition in the reaction medium with crystallites having significantly smaller sizes is induced quickly. The numerous nuclei so formed promote self-aggregation to minimize their high surface energy and readily agglomerate into larger particular aggregates (solid spherical morphology).[41] A higher processing temperature can enhance the initial nucleation as well as the aggregation process,[42,43] and thus favor the formation of initial solid aggregates observed in the temperature and time dependent studies. As evidenced from the XRD patterns, the randomly aggregated $In(OH)_3$ spheres possess poor crystallinity, and with time they undergo further reorganization and recrystallization through dissolution and redeposition. Many studies by noted groups have demonstrated that physical/chemical processes based on the Kirkendall effect and Ostwald ripening chemically induces self-transformation to form hollow structures.[13−17] The Kirkendall effect usually involves diffusion of sacrificial materials from the core, which primarily is governed by the difference in the diffusion coefficients of the materials used. In the present case, however, during the process of rapid self-aggregation smaller crystallites are usually trapped inside the cores, while the nanoparticles in the exteriors have ample time to reorient and recrystallize during the process (Scheme 1). Thus, although comprised of same constituents the smaller primary particles possessing higher curvatures intrinsically possess larger driving force to diffuse out. The nanoparticles on the outer surface of the spheres which were relatively easy to recrystallize preferentially because of availability of the solid−liquid interface,[44] serves as the new starting sites of subsequent recrystallization-reorganization processes and continued growth.[45,46] With time, thus the solid spheres transformed into a homogeneous core−shell structure, and finally the interior almost dissolved completely, until hollow spheres could be obtained with a swelled size and better crystallinity. The hollowing process corresponds to the classical theory of Ostwald ripening that involves "the growth of large crystals from those of smaller size which have a higher solubility than the larger ones".[47,48] In recent reports, this process of aging is associated with the phrase "solid-evacuation".[49]

The clues strongly indicate that hierarchical assembly of $In(OH)_3$ in solvothermal conditions thus primarily goes through several stages: (i) nucleation (primary particles), (ii) supersaturation and self-aggregation (secondary structure), and (iii) Ostwald ripening mediated by solid-evacuation and dissolution-redeposition (tertiary assembly). When the conditions and reactant composition are optimal, particularly yielding raspberry-like hollow structures, an oriented attachment mechanism is also seen to contribute during the growth of secondary architectures in the intermediate stages.

Phase Transformation of $In(OH)_3$ to In_2O_3. Studies on the phase transformation and thermal stability of hydrothermally synthesized $In(OH)_3$ architectures was carried out employing thermogravimetry (Supporting Information Figure S13). The initial weight loss observed up to 150 °C is attributed to the temperature induced desorption of physically adsorbed water molecules from the surface of as prepared materials. The most dominant second weight loss zone, that is, 150−280 °C corresponds to the removal of bound water and progressive dehydration ($2In(OH)_3 \rightarrow In_2O_3 + 3H_2O\uparrow$)[50] coupled with the loss owing to charring of residual ethanolamine and PEG moieties used during synthesis. The weight loss observed in the range 280 to 425 °C, corresponds to the completion of chemical dehydration and phase transformation process of $In(OH)_3$ to In_2O_3. Overall, this whole process of transformation to In_2O_3 was accompanied by ~21% weight loss.

Powder X-ray diffraction patterns obtained postcalcination for two characteristic $In(OH)_3$ architectures (raspberry-like hollow spheres and nanoparticle assembled spheres) at 400 °C for 3 h in a conventional oven confirmed the phase transformation to In_2O_3 (Supporting Information Figure S14). The indexed diffraction patterns matches perfectly to the *bcc*-In_2O_3 crystal structure with the space group of Ia_3 (206).[51] No characteristic peak of $In(OH)_3$ was observed, suggesting a complete phase transformation of $In(OH)_3$ to In_2O_3. Concurrently, micro-Raman measurements (Supporting Information Figure S15) were also performed on these samples to ascertain crystal structure and phase purity. The absence of Raman shift at 208, 309, 356, and 391 cm^{-1} corresponding to the *bcc*-$In(OH)_3$[52,53] corroborates phase purity achieved during transformation. The XPS and elemental analysis (Supporting Information Figures S16 and S17) substantiates the stoichiometric formation of In_2O_3. Morphological evaluations postcalcination for the In_2O_3 ascertains that it inherits the morphology and retains the hierarchical architectures of its precursor. As clearly evident from the FE-SEM images, Figure 4, although the cavities and pores along with the building blocks are seemingly more detached than observed in its parent morphology, interestingly the overall structure is preserved. Understandably, this could be attributed to the dehydration and charring of residual PEG/ethanolamine trapped within during the calcination stage.

The optical band gap (E_g, direct and indirect) of In_2O_3 (raspberry hollow sphere and nanoparticles assembled sphere morphologies) were estimated from $[F(R)\cdot h\nu]^2$ and $[F(R)\cdot h\nu]^{1/2}$ plots as a function of energy ($h\nu$) (Supporting Information Figure S18, inset). The E_g so calculated for the raspberry-like hollow spheres and nanoparticles assembled spheres are 3.38 and 3.41 eV (for direct transitions), along with

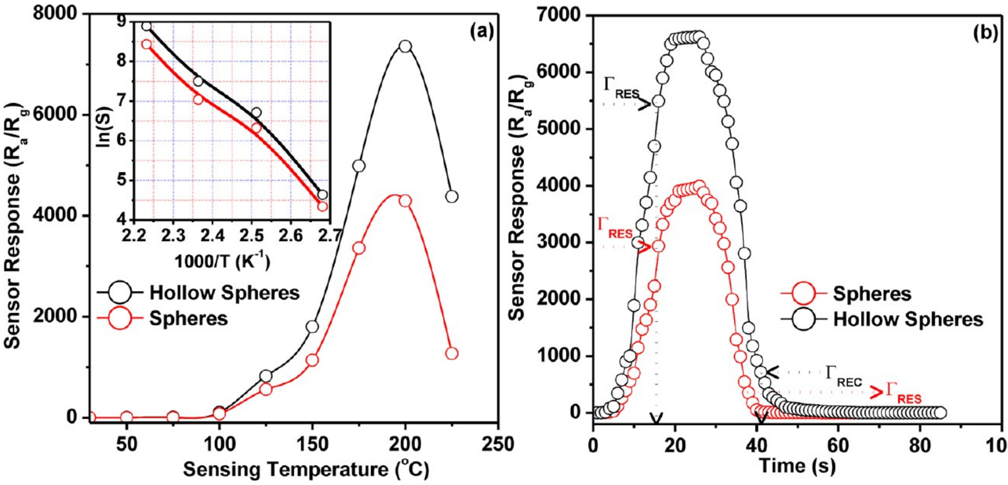

Figure 5. (a) Sensing response profiles of In_2O_3 architectures as a function of different operating temperatures toward 1% of CO. Inset: Representative Arrhenius plot depicting the sensor response. (b) Typical dynamic sensing response of In_2O_3 architectures at 200 °C toward 1% of CO.

2.85 and 2.87 eV (for indirect transitions) corresponds well with the reported values of similar In_2O_3 nanostructures.[54,55] Characteristic type-IV curves obtained (Supporting Information Figure S19) exhibits the highly mesoporous nature of the materials synthesized with an average pore size distribution of ~5−10 nm. This mesoporosity is primarily attributed to the self-assembly of primary or secondary nanostructures into hierarchical morphologies. The calculated surface area (Supporting Information Figure S20) of raspberry-like hollow spheres and primary nanoparticle assembled spheres are 91 and 82 m^2/g, respectively.

Gas Sensor Fabrication and Measurements. One of the most effective demonstrations to showcase the application of nanostructured metal-oxides is chemical gas sensing.[56−58] Mesoporosity coupled with controlled architectures is envisaged to enhance gas sensing performance multifold. Several prior arts have shown the feasibility of In_2O_3 as a promising gas sensing material particularly with reference to carbon monoxide (CO). One of the most harmful and toxic among the pollutants, CO reacts rapidly with human blood hemoglobin to form carboxy-hemoglobin and causes asphyxation.[59,60] The merits of achieving the exotic hierarchical architectures with considerable mesoporosity as discussed in the preceding sections were hence justified following a comprehensive study on their CO sensing and performance.

Schematics of the sensor assembly, techniques used for fabrication and experimental setup have all been extensively described in our previous reports.[61,62] The In_2O_3 sensing element fabricated using raspberry-like hollow spheres and nanoparticles assembled spheres were tested as a function of temperature in a dry air environment. To determine the thermally activated conditions where adsorption/desorption kinetics is optimum the sensor response was followed as a function of temperature toward 1% of CO. Figure 5a shows the typical sensing response of two hierarchical In_2O_3 architectures as a function of temperature (T_s). The sensing characteristics show a typical n-type behavior, that is, decrease in sensor resistance when exposed to reducing gas. The sensor response at lower temperatures were observed to be significantly less which can be primarily attributed to the low concentration of active oxygen species available on the metal oxide surface. Coupled to this, the thermal activation for CO molecules to react with surface oxygen species is also understandably slower. With increase in temperature the response increases showing an optimal response at ~200 °C and thereafter the response decreases again owing to various trade-offs. At the optimum sensing temperature (200 °C), the maximum sensor response (S_{max}) exhibited by the raspberry-like hollow spheres is ~7340, while for the nanoparticle assembled spheres, $S_{max} \approx 4055$. Inset in Figure 5a presents the Arrhenius plots clearly indicating the linear dependence of sensor response as a function of operating temperature ($\ln(S)$ vs T_s). The dynamic sensor response, which follows the response and recovery as a function of time is also depicted for the two typical sensing elements at 200 °C toward 1% CO (Figure 5 (b)). The estimated response (Γ_{RES}) and recovery (Γ_{REC}) times are found to be $\Gamma_{RES} \approx 15$ s and $\Gamma_{REC} \approx 16$ s for raspberry-like hollow spheres, while $\Gamma_{RES} \approx 16$ s and $\Gamma_{REC} \approx 15$ s for nanoparticles assembled spheres, respectively.

Dynamic sensor response of In_2O_3 raspberry-like hollow spheres and nanoparticles assembled spheres were also investigated as a function of CO concentration in air (100, 50, 20, 10, 5, 2, 1 ppm) at 200 °C to ascertain limit of sensitivity (Figure 6). As evident from the analysis the In_2O_3 architectures not only shows a wide range of detection limit but also appreciably quick response (Γ_{RES})/recovery (Γ_{REC}) time. In_2O_3 raspberry-like hollow spheres showed a maximum sensor responses (S_{max}) of 96, 69, 37, 22, 14, 11, 7, while for the nanoparticles assembled spheres S_{max} observed were ~81, 58, 30, 19, 10, 6, 4 for 100, 50, 20, 10, 5, 2, 1 ppm of CO in air, respectively. The linear plots of $\ln(S_g - 1)$ as a function of gas concentration shown as inset in Figure 6a and b summarizes the findings.

Gas Sensing Mechanism. The excellent CO sensing response observed for these hierarchical In_2O_3 architectures synthesized can be rationalized considering the following major factors that play key roles. First, the morphology of In_2O_3 architectures (mesoporous raspberry like hollow spheres and nanoparticles assembled spheres) undoubtedly offers considerable advantage. As highlighted in the preceding sections, the architectures are composed of numerous ultrafine nanoparticles that remarkably enhance the depletion regions of the sensing element. Such conditions are most desirable for an ultrahigh sensing response.[63] Second, the exemplary mesoporosity

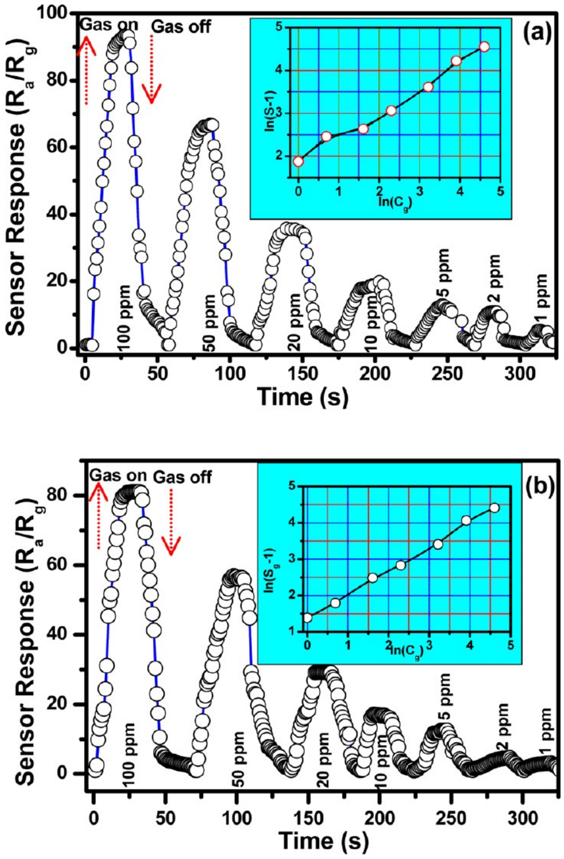

Figure 6. Dynamic sensor response of In_2O_3 as a function of different gas concentrations at operating temperature of 200 °C (a) raspberry hollow spheres and (b) nanoparticle-assembled spheres.

coupled with higher specific surface area (~91 and ~82 m^2/g) provides for the ease of gas diffusion and more active sites for the formation of reactive oxygen species. At elevated temperatures, the oxygen chemisorbed on the sensing element produces the numerous reactive oxygen species (O^{2-}, O_2^-, O^-) which causes a decrease in the carrier concentration, resulting in increased resistance of the material. When the sensing element is exposed to CO, a fast chemical reaction that consumes the reactive oxygen species takes place on the sensor element surface producing CO_2 while releasing the electrons. This surge of released electrons following the reaction leads to an increase in the carrier concentration and a sudden decrease in the resistance. The mechanism can be put forth in the following simple chemical reactions.[64]

$$O_2(\text{gas}) \rightarrow O_2(\text{ad}) \tag{1}$$

$$O_2(\text{ad}) + e^- \rightarrow O_2(\text{ad})^- \tag{2}$$

$$O_2(\text{ad})^- + e^- \rightarrow 2O(\text{ad})^- \tag{3}$$

$$CO + O_2(\text{ad})^- + e^- \rightarrow CO_2(\text{gas}) + e^- \tag{4}$$

Photocatalytic Efficiency of In_2O_3 Architectures. Nanostructured materials have equally impacted the area of catalysis and as such semiconducting metal-oxides in particular have been of significant interest in the area of photocatalysis. The photocatalytic performances of these hierarchical In_2O_3 architectures (raspberry hollow spheres and nanoparticles assembled spheres) were hence explored with degradation studies on a well studied model system, Rhodamine B under UV-light illumination at room temperature.

The absorption spectra of Rhodamine B in the presence of In_2O_3 photocatalyst obtained under different reaction times are

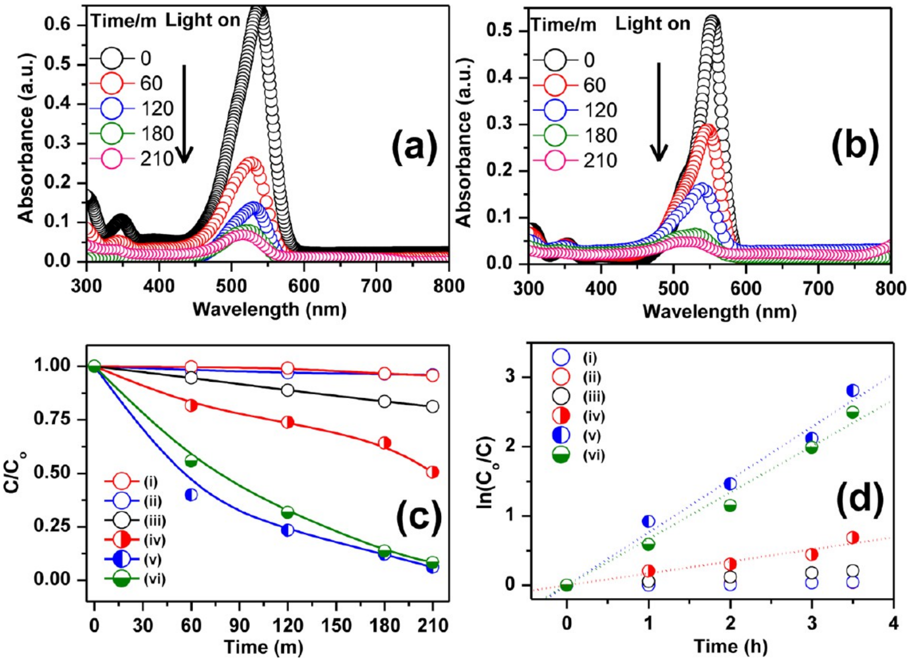

Figure 7. UV−visible absorbance spectra depicting the change in concentration of the dye, RhB solution in the presence of In_2O_3 under UV irradiation as a function of time. (a) Raspberry-like hollow spheres (RHS). (b) Nanoparticle-assembled spheres (NPAS). (c) Normalized photocatalytic degradation of RhB as a function of time: (i) adsorption on raspberry-like hollow spheres under dark, (ii) adsorption on nanoparticles assembled spheres under dark, (iii) without catalyst under light, (iv) degradation on c-In_2O_3 (commercial sample), (v) degradation on raspberry-like hollow spheres, and (vi) degradation on nanoparticles assembled spheres. (d) Estimation of rate constants from the linear fits to the experimental data.

provided in Figure 7a and b. The UV-spectra of aliquots drawn from the reaction mix at different time intervals clearly shows that the peak at λ_{max} of 540 nm steadily decreases with increasing illumination time indicating Rhodamine B degradation. Figure 7c depicts the approximate linear relationship of C/C_o versus the irradiation time, t. At sufficiently low concentration of the substrate, the photodegradation process of RhB can be approximated to Langmuir−Hinshelwood first-order kinetics. This can be expressed as follows: $\ln(C_o/C) = kt$, where k is the degradation reaction rate constant, C_o and C are the initial concentration and the concentration at reaction time, t, respectively.[65] When Rhodamine B/In_2O_3 suspensions were irradiated for 210 min the degradation efficiency is about 93% for raspberry hollow spheres and 91% for nanoparticles assembled spheres, respectively. The degradation rate constants estimated for the raspberry hollow spheres and nanoparticles assembled spheres are found to be 0.76 and 0.67 against 0.17 for commercially available material (c-In_2O_3, SRL make, India) as a control. These experimental findings definitely reveal the superior photocatalytic performance of these hierarchically structured In_2O_3 materials synthesized. Usually, the photocatalytic efficiency of semiconductors is primarily dependent on the photogeneration followed by electron−hole pairs separation. The ease of transfer of electrons from the substrate to the reactant also determines the efficiency of the photocatalyst. This apart, in the present study, the size and surface area of the materials also do play a key role that enhances the photocatalytic performance. The ultrafine nanoparticles are responsible to reduce the recombination rate of electron−hole pairs and promote charge separation. The high specific surface area (raspberry hollow spheres ~91 m^2/g and nanoparticles assembled spheres ~82 m^2/g) provides added advantage by increasing the effective absorption and number of reaction sites. The initial findings of this study, albeit with a well studied model system showcasing degradation of RhB, however, implies the huge potential these hierarchical structures may have in classical organic transformations.

■ CONCLUSION

In summary, we have successfully demonstrated a solvothermal synthetic strategy to obtain exotic hierarchical structures of mesoporous $In(OH)_3$ with impressive reproducibility that can be achieved exercising simple constraints. Appreciable control on the morphology and self-assembly of nanostructures can be exercised by manipulating the reactant concentration, mixed solvent system (DMF:PEG), ratio of structure directing agents in the reaction medium (PEG, EA), water content, the reaction temperature, and time. Detailed investigation employing electron microscopy coupled with X-ray diffraction analysis provided significant clues relevant to the evolution of these superstructures. The key stages of formation, phases involved at each stage, involvement of the primary and a secondary structure that leads to the hierarchical tertiary assemblies were comprehensively discerned following controlled studies as a function of various reaction parameters. The morphological evolution observed could be rationally correlated with the nucleation, growth, oriented attachment, and Ostwald ripening aided by dissolution-redeposition mechanism assisted by solid evacuation to propose a plausible formation mechanism. Thermal transformation of these nanostructures to In_2O_3 postsynthesis were also achieved successfully while retaining their original morphology. The findings from XRD, TGA, micro- Raman, and UV-DRS analysis were consistent with each other. Estimation of surface area and pore size distribution of the as prepared nanostructures exhibit considerably high surface area (91 and 82 m^2/g) with significant mesoporosity (pore size ~5−10 nm). To showcase the performance enhancement that can be achieved by tailoring the nanostructures, two typical hierarchical structures (raspberry-like hollow spheres and nanoparticles assembled spheres) were investigated for their gas sensing and photocatalytic performances. The influences of In_2O_3 morphology on the CO gas sensing properties were investigated comprehensively evaluating the sensitivity, sensor response and recovery time with respect to carbon monoxide concentration. At an optimum working temperature (~200 °C), encouraging sensor response, $S_{max} \approx 7340$ and 4055 were exhibited by In_2O_3 raspberry-like hollow spheres and nanoparticles assembled spheres, respectively. Impressively fast response/recovery times over a wide concentration range and as low as 1 ppm exhibit superior sensitivity. The initial findings of photocatalytic activity with a model system RhB to study degradation of dye molecules implies the huge potential these hierarchical structures may have in classical organic transformations. When compared to commercial In_2O_3, the pseudo-first-order rate constants estimated indicated approximately a 3−4 times enhancement in substrate reactivity. The excellent sensor response and photocatalytic activity is undoubtedly facilitated by the presence of smaller primary nanostructures offering numerous reactive sites coupled with considerable mesoporosity and hollow architectures that facilitates rapid diffusion and faster adsorption−desorption kinetics.

■ ASSOCIATED CONTENT

Ⓢ Supporting Information

Details of experimental methods and characterization techniques; gas sensor fabrication and measurements; photocatalytic studies; powder X-ray diffraction patterns, additional FE-SEM images; supplementary discussions pertaining to formation mechanisms; thermo-gravimetry analysis; micro-Raman spectroscopy analysis; UV-DRS spectra; EDX and XPS analysis; N_2 adsorption−desorption isotherms and corresponding BJH pore size distributions of these hierarchical architectures; UV−visible spectroscopic changes of the aqueous RhB solution in the absence of In_2O_3 photocatalyst and for commercial In_2O_3. This material is available free of charge via the Internet at http://pubs.acs.org.

■ AUTHOR INFORMATION

Corresponding Authors

*Tel: +91-40-27193225. Fax: +91-40-27160921. E-mail: pratyay@iict.res.in
*E-mail: manorama@iict.res.in.

Notes

The authors declare no competing financial interest.

■ ACKNOWLEDGMENTS

A.K.S. acknowledges the Council of Scientific and Industrial Research (CSIR), India, for the Senior Research Fellowship (SRF). P.B. and S.V.M. duly acknowledge the strong support of MNRE-CSIR TAPSUN Project on Dye Sensitized Solar Cells (*Dye*Cell: GAP-0366) and the CSIR XII-FYP Project M2D (CSC-0134) for the grants received.

REFERENCES

(1) Fang, X.; Liu, Z.; Hsieh, M.-F.; Chen, M.; Liu, P.; Chen, C.; Zheng, N. Hollow Mesoporous Aluminosilica Spheres with Perpendicular Pore Channels as Catalytic Nanoreactors. *ACS Nano* **2012**, *6*, 4434−4444.

(2) Goldberger, J.; He, R.; Zhang, Y.; Lee, S.; Yan, H.; Choi, H.-J.; Yang, P. Single-Crystal Gallium Nitride Nanotubes. *Nature* **2003**, *422*, 599−602.

(3) Lou, X. W.; Archer, L. A.; Yang, Z. Hollow Micro-/Nanostructures: Synthesis and Applications. *Adv. Mater.* **2008**, *20*, 3987−4019.

(4) Djojoputro, H.; Zhou, X. F.; Qiao, S. Z.; Wang, L. Z.; Yu, C. Z.; Lu, G. Q. Periodic Mesoporous Organosilica Hollow Spheres with Tunable Wall Thickness. *J. Am. Chem. Soc.* **2006**, *128*, 6320−6321.

(5) Caruso, F.; Caruso, R. A.; Mohwald, H. Nanoengineering of Inorganic and Hybrid Hollow Spheres by Colloidal Templating. *Science* **1998**, *282*, 1111−1114.

(6) Zhang, Q.; Lee, I.; Ge, J.; Zaera, F.; Yin, Y. Surface-Protected Etching of Mesoporous Oxide Shells for the Stabilization of Metal Nanocatalysts. *Adv. Funct. Mater.* **2010**, *20*, 2201−2214.

(7) Zhong, Z.; Yin, Y.; Gates, B.; Xia, Y. Preparation of Mesoscale Hollow Spheres of TiO_2 and SnO_2 by Templating Against Crystalline Arrays of Polystyrene Bead. *Adv. Mater.* **2000**, *12*, 206−209.

(8) Kamata, K.; Lu, Y.; Xia, Y. Synthesis and Characterization of Monodispersed Core−Shell Spherical Colloids with Movable Cores. *J. Am. Chem. Soc.* **2003**, *125*, 2384−2385.

(9) Wu, M.; Wang, G.; Xu, H.; Long, J.; Shek, F. L. Y.; Lo, S. M. -F.; Williams, I. D.; Feng, S.; Xu, R. Hollow Spheres Based on Mesostructured Lead Titanate with Amorphous Framework. *Langmuir* **2003**, *19*, 1362−1367.

(10) Wong, Y. J.; Zhu, L. F.; Teo, W. S.; Tan, Y. W.; Yang, Y. H.; Wang, C.; Chen, H. Y. Revisiting the Stöber Method: Inhomogeneity in Silica Shells. *J. Am. Chem. Soc.* **2011**, *133*, 11422−11425.

(11) Teng, Z.; Su, X.; Zheng, Y.; Sun, J.; Chen, G.; Tian, C.; Wang, J.; Li, H.; Zhao, Y.; Lu, G. Mesoporous Silica Hollow Spheres with Ordered Radial Mesochannels by a Spontaneous Self-Transformation Approach. *Chem. Mater.* **2013**, *25*, 98−105.

(12) Lv, R.; Gai, S.; Dai, Y.; Niu, N.; He, F.; Yang, P. Highly Uniform Hollow GdF_3 Spheres: Controllable Synthesis, Tuned Luminescence, and Drug-Release Properties. *ACS Appl. Mater. Interfaces* **2013**, *5*, 10806−10818.

(13) Zhang, G.; Wang, W.; Yu, Q.; Li, X. Facile One-Pot Synthesis of PbSe and $NiSe_2$ Hollow Spheres: Kirkendall-Effect-Induced Growth and Related Properties. *Chem. Mater.* **2009**, *21*, 969−974.

(14) Nakamura, R.; Tokozakura, D.; Nakajima, H.; Lee, J. G.; Mori, H. Hollow Oxide Formation by Oxidation of Al and Cu Nanoparticles. *J. Appl. Phys.* **2007**, *101*, 074303−074307.

(15) Shao, H. F.; Qian, X. F.; Zhu, Z. K. The Synthesis of ZnS Hollow Nanospheres with Nanoporous Shell. *J. Solid State Chem.* **2005**, *178*, 3522−3528.

(16) Wang, Y.; Cai, L.; Xia, Y. Monodisperse Spherical Colloids of Pb and Their Use as Chemical Templates to Produce Hollow Particles. *Adv. Mater.* **2005**, *17*, 473−477.

(17) Ma, Y. W.; Huo, K. F.; Wu, Q.; Lu, Y. N.; Hu, Y. M.; Hu, Z.; Chen, Y. Self-Templated Synthesis of Polycrystalline Hollow Aluminium Nitride Nanospheres. *J. Mater. Chem.* **2006**, *16*, 2834−2838.

(18) Ho, C.-H.; Chan, C.-H.; Tien, L.-C.; Huang, Y.-S. Direct Optical Observation of Band-Edge Excitons, Band Gap, and Fermi Level in Degenerate Semiconducting Oxide Nanowires In_2O_3. *J. Phys. Chem. C* **2011**, *115*, 25088−25096.

(19) Epifani, M.; Siciliano, P. Ambient Pressure Synthesis of Corundum-Type In_2O_3. *J. Am. Chem. Soc.* **2004**, *126*, 4078−4079.

(20) Zhang, D.; Liu, Z.; Li, C.; Tang, T.; Liu, X.; Han, S.; Lei, B.; Zhou, C. Detection of NO_2 Down to ppb Levels Using Individual and Multiple In_2O_3 Nanowire Devices. *Nano Lett.* **2004**, *4*, 1919−1924.

(21) Xu, L.; Dong, B.; Wang, Y.; Bai, X.; Chen, J.; Liu, Q.; Song, H. Porous In_2O_3:RE (RE: Gd, Tb, Dy, Ho, Er, Tm, Yb) Nanotubes: Electrospinning Preparation and Room Gas-Sensing Properties. *J. Phys. Chem. C* **2010**, *114*, 9089−9095.

(22) Shi, M.; Xu, F.; Yu, K.; Zhu, Z.; Fang, J. Controllable Synthesis of In_2O_3 Nanocubes, Truncated Nanocubes, and Symmetric Multipods. *J. Phys. Chem. C* **2007**, *111*, 16267−16271.

(23) Yang, H.; Zhang, R.; Dong, H.; Yu, J.; Yang, W.; Chen, D. In Situ Growth of Self-Assembled and Single In_2O_3 Nanosheets on the Surface of Indium Grains. *Cryst. Growth Des.* **2008**, *8*, 3154−3159.

(24) Dong, H.; Chen, Z.; Sun, L.; Zhou, L.; Ling, Y.; Yu, C.; Tan, H. H.; Jagadish, C.; Shen, X. Nanosheets-Based Rhombohedral In_2O_3 3D Hierarchical Microspheres: Synthesis, Growth Mechanism, and Optical Properties. *J. Phys. Chem. C* **2009**, *113*, 10511−10516.

(25) Zai, J.; Zhu, J.; Qi, R.; Qian, X. Nearly Monodispersed $In(OH)_3$ Hierarchical Nanospheres and Nanocubes: Tunable Ligand-Assisted Synthesis and Their Conversion into Hierarchical In_2O_3 for Gas Sensing. *J. Mater. Chem. A* **2013**, *1*, 735−745.

(26) Sun, X.; Hao, H.; Ji, H.; Li, X.; Cai, S.; Zheng, C. Nanocasting Synthesis of In_2O_3 with Appropriate Mesostructured Ordering and Enhanced Gas-Sensing Property. *ACS Appl. Mater. Interfaces* **2014**, *6*, 401−409.

(27) Kim, S.-J.; Hwang, I.-S.; Na, C. W.; Kim, I.-D.; Kang, Y. C.; Lee, J.-H. Ultrasensitive and Selective C_2H_5OH Sensors Using Rh-Loaded In_2O_3 Hollow Spheres. *J. Mater. Chem.* **2011**, *21*, 18560−18567.

(28) Li, B.; Yi, X.; Jing, M.; Rong, G.; Tang, Y.; Zhang, G. In_2O_3 Hollow Microspheres: Synthesis from Designed $In(OH)_3$ Precursors and Applications in Gas Sensors and Photocatalysis. *Langmuir* **2006**, *22*, 9380−9385.

(29) Chen, L.-Y.; Zhang, Z.-D. Biomolecule-Assisted Synthesis of $In(OH)_3$ Hollow Spherical Nanostructures Constructed with Well-Aligned Nanocubes and Their Conversion into C-In_2O_3. *J. Phys. Chem. C* **2008**, *112*, 18798−18803.

(30) Yu, J.; Guo, H.; Davis, S. A.; Mann, S. Fabrication of Hollow Inorganic Microspheres by Chemically Induced Self-Transformation. *Adv. Funct. Mater.* **2006**, *16*, 2035−2041.

(31) Kong, F. Y.; Li, M.; Yao, X. Y.; Xu, J. M.; Wang, A. D.; Liu, Z. P.; Li, G. H. Template-Free Hydrothermal Synthesis of VO_2 Hollow Microspheres. *CrystEngComm.* **2012**, *14*, 3858−3861.

(32) Wu, Q.; Chen, J.; Zhang, F.; Xiao, P.; Lu, Y.; Wang, X.; Hu, Z. Anion-Induced Morphological Regulation of $In(OH)_3$ Nanostructures and Their Conversion into Porous In_2O_3 Derivatives. *CrystEngComm.* **2012**, *14*, 3397−3403.

(33) Du, J.; Yang, M.; Cha, S. N.; Rhen, D.; Kang, M.; Kang, D. J. Indium Hydroxide and Indium Oxide Nanospheres, Nanoflowers, Microcubes, and Nanorods: Synthesis and Optical Properties. *Cryst. Growth Des.* **2008**, *8*, 2312−2317.

(34) Shanmugasundaram, A.; Ramireddy, B.; Basak, P.; Manorama, S. V.; Srinath, S. Hierarchical $In(OH)_3$ as a Precursor to Mesoporous In_2O_3 Nanocubes: A Facile Synthesis Route, Mechanism of Self-Assembly, and Enhanced Sensing Response toward Hydrogen. *J. Phys. Chem. C* **2014**, *118*, 6909−6921.

(35) Wang, W.-S.; Liang, Z.; Xu, C.-Y.; Chen, J.-Z.; Shao, W.-Z. Aqueous Solution Synthesis of CaF_2 Hollow Microspheres via the Ostwald Ripening Process at Room Temperature. *ACS Appl. Mater. Interfaces* **2009**, *1*, 780−788.

(36) Gao, D.; Zhang, X.; Gao, W. Formation of Bundle-Shaped β-$NaYF_4$ Up Conversion Microtubes via Ostwald Ripening. *ACS Appl. Mater. Interfaces* **2013**, *5*, 9732−9739.

(37) Zhong, Y.; Su, L.; Yang, M.; Wei, J.; Zh, Z. Rambutan-Like $FeCO_3$ Hollow Microspheres: Facile Preparation and Superior Lithium Storage Performances. *ACS Appl. Mater. Interfaces* **2013**, *5*, 11212−11217.

(38) Shang, S.; Jiao, X.; Chen, D. Template-Free Fabrication of TiO_2 Hollow Spheres and Their Photocatalytic Properties. *ACS Appl. Mater. Interfaces* **2012**, *4*, 860−865.

(39) Zhou, X.; Chen, S.; Zhang, D.; Guo, X.; Ding, W.; Chen, Yi. Microsphere Organization of Nanorods Directed by PEG Linear Polymer. *Langmuir* **2006**, *22*, 1383−1387.

(40) Zhang, Q. L. *Inorganic Chemistry Series*; Science Press: Beijing, 1998.

DOI: 10.1021/acsami.5b00584
ACS Appl. Mater. Interfaces 2015, 7, 7679−7689

(41) Li, D.; Qin, Q.; Duan, X.; Yang, J.; Guo, W.; Zheng, W. General One-Pot Template-Free Hydrothermal Method to Metal Oxide Hollow Spheres and Their Photocatalytic Activities and Lithium Storage Properties. *ACS Appl. Mater. Interfaces* **2013**, *5*, 9095−9100.

(42) Tian, X. L.; Li, J.; Chen, K.; Han, J.; Pan, S. L.; Wang, Y. J.; Fan, X. Y.; Li, F.; Zhou, Z. X. Nearly Monodisperse Ferroelectric $BaTiO_3$ Hollow Nanoparticles: Size-Related Solid Evacuation in Ostwald-Ripening-Induced Hollowing Process. *Cryst. Growth Des.* **2010**, *10*, 3990−3995.

(43) Li, S.; Wu, Z.; Li, W.; Liu, Y.; Zhuo, R.; Yan, D.; Jun, W.; Yan, P. One-Pot Synthesis of ZnS Hollow Spheres via a Low-Temperature, Template-Free Hydrothermal Route. *CrystEngComm.* **2013**, *15*, 1571−1577.

(44) Ye, T.; Dong, Z.; Zhao, Y.; Yu, J.; Wang, F.; Guo, S.; Zou, Y. Controllable Fabrication of Perovskite $SrZrO_3$ Hollow Cuboidal Nanoshells. *CrystEngComm.* **2011**, *13*, 3842−3847.

(45) Wu, M.; Zhang, X.; Gao, S.; Cheng, X.; Rong, Z.; Xu, Y.; Zhao, H.; Huo, L. Construction of Monodisperse Vanadium Pentoxide Hollow Spheres via a Facile Route and Triethylamine Sensing Property. *CrystEngComm.* **2013**, *15*, 10123−10131.

(46) Lou, X. W.; Wang, Y.; Yuan, C. L.; Lee, J. Y.; Archer, L. A. Template-Free Synthesis of SnO Hollow Nanostructures with High Lithium Storage Capacity. *Adv. Mater.* **2006**, *18*, 2325−2329.

(47) Pan, A. Q.; Wu, H. B.; Yu, L.; Lou, X. W. Template-Free Synthesis of VO Hollow Microspheres with Various Interiors and Their Conversion into V_2O_5 for Lithium-Ion Batteries. *Angew. Chem., Int. Ed.* **2013**, *52*, 2226−2230.

(48) Yu, X.-Y.; Yao, X.-Z.; Luo, T.; Jia, Y.; Liu, J.-H.; Huang, X.-J. Facile Synthesis of Urchin-like $NiCo_2O$ Hollow Microspheres with Enhanced Electrochemical Properties in Energy and Environmentally Related Applications. *ACS Appl. Mater. Interfaces* **2014**, *6*, 3689−3695.

(49) Liu, J.; Liu, F.; Gao, K.; Wu, J.; Xue, D. Recent Developments in the Chemical Synthesis of Inorganic Porous Capsules. *J. Mater. Chem.* **2009**, *19*, 6073−6084.

(50) Patra, C. R.; Gedanken, A. Rapid Synthesis of Nanoparticles of Hexagonal Type In_2O_3 and spherical type Tl_2O_3 by Microwave Irradiation. *New. J. Chem.* **2004**, *28*, 1060−1065.

(51) Mu, J.; Chen, B.; Zhang, M.; Guo, Z.; Zhang, P.; Zhang, Z.; Sun, Y.; Shao, C.; Liu, Y. Enhancement of the Visible-Light Photocatalytic Activity of In_2O_3−TiO_2 Nanofiber Heteroarchitectures. *ACS Appl. Mater. Interfaces* **2012**, *4*, 424−430.

(52) Gai, L.; Ma, L.; Jiang, H.; Ma, Y.; Tian, Y.; Liu, H. Nitrogen-Doped In_2O_3 Nanocrystals Constituting Hierarchical Structures with Enhanced Gas-Sensing Properties. *CrystEngComm.* **2012**, *14*, 7479−7486.

(53) Yang, J.; Frost, R. L.; Martens, W. N. Thermogravimetric Analysis and Hot-Stage Raman Spectroscopy of Cubic Indium Hydroxide. *J. Therm. Anal. Calorim.* **2009**, *100*, 109−116.

(54) Goyal, R. P.; Raviendra, D.; Gupta, B. R. K. Electroless Deposition of In_2O_3 and In_2O_3:Sn(ITO). *Phys. Status Solidi A* **1985**, *87*, 79−83.

(55) Qiu, Y.; Bellina, P.; Jeurgens, L. P. H.; Leineweber, A.; Welzel, U.; Gerstel, P.; Jiang, L.; Aken, P. A. V.; Bill, J.; Aldinger, F. Aqueous Deposition of Ultraviolet Luminescent Columnar Tin-Doped Indium Hydroxide Films. *Adv. Funct. Mater.* **2008**, *18*, 2572−2583.

(56) Yamazoe, N. New Approaches for Improving Semiconductor Gas Sensors. *Sens. Actuators, B* **1991**, *5*, 7−19.

(57) Sberveglieri, G. Recent Developments in Semiconducting Thin-Film Gas Sensors. *Sens. Actuators, B* **1995**, *23*, 103−109.

(58) Kolmakov, A.; Zhang, X. Y.; Cheng, G. S.; Moskovits, M. Detection of CO and O_2 Using Tin Oxide Nanowire Sensors. *Adv. Mater.* **2003**, *15*, 997−1000.

(59) Zhang, T.; Liu, L.; Qi, Q.; Li, S.; Lu, G. Development of Microstructure In/Pd-Doped SnO_2 Sensor for Low-Level CO Detection. *Sens. Actuators, B* **2009**, *139*, 287−291.

(60) Krishnakumar, T.; Jayaprakash, R.; Pinna, N.; Donato, F. N.; Bonavita, A.; Micali, G.; Neri, G. CO Gas Sensing of ZnO Nanostructures Synthesized by an Assisted Microwave wet Chemical Route. *Sens. Actuators, B* **2009**, *143*, 198−204.

(61) Baruwati, B.; Kumar, D. K.; Manorama, S. V. Hydrothermal Synthesis of Highly Crystalline ZnO Nanoparticles: A Competitive Sensor for LPG and EtOH. *Sens. Actuators, B* **2006**, *119*, 676−682.

(62) Shanmugasundaram, A.; Basak, P.; Satyanarayana, L.; Manorama, S. V. Hierarchical SnO/SnO_2 Nanocomposites: Formation of in situ p−n Junctions and Enhanced H_2 Sensing. *Sens. Actuators, B* **2013**, *185*, 265−273.

(63) Liu, H.; Gong, S. P.; Hu, Y. X. J.; Liu, Q.; Zhou, D. X. Properties and Mechanism Study of SnO_2 Nanocrystals for H_2S Thick-Film Sensors. *Sens. Actuators, B* **2009**, *140*, 190−195.

(64) Amin, M.; Shah, N. A.; Bhatti, A. S.; Malik, M. A. Effects of Mg Doping on Optical and CO Gas Sensing Properties of Sensitive ZnO Nanobelts. *CrystEngComm.* **2014**, *16*, 6080−6088.

(65) Su, C.; Liu, L.; Zhang, M.; Zhang, Y.; Shao, C. Fabrication of Ag/TiO_2 Nanoheterostructures with Visible Light Photocatalytic Function via a Solvothermal Approach. *CrystEngComm.* **2012**, *14*, 3989−3999.